Bulletin of the Seismological Society of America, Vol. 102, No. 2, pp. 802–811, April 2012, doi: 10.1785/0120110091

Geometric Seismic-Wave Inversion by the Boundary Element Method

by Samuel Bignardi, Francesco Fedele,* Anthony Yezzi, Glenn Rix, and Giovanni Santarato

Abstract Surface-wave methods are widely used in earth sciences and engineering for the geometric characterization of geological bodies and tectonic structures of the subsurface. These techniques exploit the dispersive nature of Rayleigh waves to indirectly estimate shear wave velocity profiles from surface-wave measurements; however, they are limited to parallel-layered geometries. To overcome such limitations, we present a new class of geometric inverse models for a full waveform inversion (FWI) based on the boundary element method (BEM). The proposed approach enables an effective identification of two dimensional (2D) subsurface geometries by directly estimating the shape of laterally varying interfaces from raw measurements. It thus aims at filling the gap between the standard simplistic parallel-layered-based inversion and that of more complex three-dimensional (3D) geometries based on finite element methods (FEMs). Numerical tests on synthetic data unveil the effectiveness of the inverse algorithm, and its applicability to field measurements is finally presented.

Introduction

The geometric characterization of geological bodies and tectonic structures of the subsurface is a crucial issue in many fields of earth sciences and engineering, and particularly for seismic hazard assessment. Indeed, a good geological knowledge of the subsurface allows researchers to predict local seismic effects for microzonation at large scales $\sim O(10^3)$ m (sedimentary basins or alluvial valleys) or to locate with sufficient precision a fault trace and provide useful information for antiseismic management plans at smaller scales. Direct investigations, such as drilling or excavations, yield pointwise information of the subsurface, but they are very expensive, even at the metric-to-decametric scale. Common alternative methods are based on the analysis of passive (natural) or active (artificial) seismic waves. In particular, in recent years surface wave methods (SWMs) have been widely used to reveal subsurface properties, especially those of S waves in shallow depths (~30 m), which are relevant for planning any construction in areas prone to seismic risk.

Surface wave methods utilize the dispersive nature of Rayleigh waves in a vertically heterogeneous half-space to obtain the shear wave velocity profile from the wave particle motions excited and recorded on the ground surface. To date, many variations of the basic test and inversion protocol exist, such as the two-receiver approach based on the spectral analysis of surface waves (Nazarian *et al.*, 1984; Stokoe *et al.*, 1994) and the multichannel method that exploits arrays of receivers (e.g., Gabriels *et al.*, 1987; Tokimatsu, 1995; Tselentis and Delis, 1998; Park *et al.*, 1999; Strobbia and Foti, 2006). Other techniques utilize passively generated surface waves to increase penetration depth (Louie, 2001; Rix *et al.*, 2002; Park *et al.*, 2005) and to enable inversions of soil damping ratios via measurements of wave attenuation (Rix *et al.*, 2000, 2001; Lai *et al.*, 2002).

The inverse problem at the root of SWMs requires a forward model to solve the propagation, scattering, and dissipation of seismic waves through the medium. This is idealized as a sequence of flat, horizontal, isotropic, and homogeneous layers. Such models are capable of capturing only a discrete vertical variation in elastic properties, that is, they are one dimensional (1D). One of their attractive features is that they are computationally efficient to calculate the modal displacements and tractions using matrix operations (Kausel and Roesset, 1981; Aki and Richards, 2002), which makes such models ideal for inverse problems employing iterative solutions. Clearly, however, this model is only an approximation of the actual subsurface conditions for most sites, and it may yield misleading results if the actual soil profile is far from the assumed geometry. Indeed, the major drawback is that wave propagation is modeled as the linear superposition of dispersive Rayleigh modes that do not interfere or diffract as they would if the profile were not horizontally layered. Observations and modeling of earthquakes confirm, for example, that seismic waves can be amplified at alluvial valley edges, and diffraction effects can be observed because the interface between soft sediments and bedrock is far from being horizontal (Bard and Gabriel, 1986; Aki, 1988; Kawase, 1988; Kawase and Aki, 1989). Furthermore, surface topography can alter

*Also at School of Civil and Environmental Engineering, Georgia Institute of Technology, 225 North Avenue NW, Atlanta, Georgia 30332.

seismic wave propagation (Bard, 1982; Raptakis *et al.*, 2000; Assimaki and Kausel, 2007). In particular, amplification is usually expected at hilltops (Bard, 1982), and complex amplified and deamplified patterns occur at hill flanks (Savage, 2004).

Several attempts have been made to model lateral variations via the so-called pseudo-2D inversion (e.g., Luo *et al.*, 2008), in which successive 1D inversions along the length of the survey are combined via interpolation or other type of smoothing kernel; however, this approach is inherently limited. Analytical solutions of forward models for true 2D and 3D media are available, but only for a very restricted class of weakly varying layered geometries (Gjevik, 1973; Maupin and Kennett, 1987; Dravinski and Mossessian 1997; Maupin, 2007). As such, these solutions are of limited practical value.

Thus, the further maturation of SWMs has been limited by the lack of effective and efficient computational models that enable more realistic representations of 2D/3D subsurface media. Only recently, for crustal and lithospheric scale structures have such limitations been overcome by a full seismic waveform inversion (FWI) methodology that combines an effective forward model based on the finite element method (FEM) to model seismic wave propagation and adjoint techniques to efficiently compute the gradient of the data misfit functional to perform minimization (e.g., Virieux and Operto, 2009; Fichtner, 2010). When an FEM forward model is used, complex media are finely discretized into a large number of nodes or 3D volume elements. Each node is associated with an unknown parameter, which characterizes the soil seismic property at that node location. Typically, the number of parameters to be estimated largely exceeds the number of measurements available by several orders of magnitude; thus, the inverse problem is severely ill-posed. Ill-posedness is usually treated by regularization procedures (Tikhonov and Arsenin, 1977; Tarantola, 1987) by including additional constraints that yield well-posed inverse algorithms. The shortcoming is that, as with most nonlinear inverse methods, these approaches suffer from slow convergence and instability. Indeed, it is well known that a good starting model is needed in FWI, and generally in inverse methods, to avoid false positives (i.e., false result indications) that may arise because local optimization does not prevent convergence of the misfit function toward local minima.

In this paper, we propose an alternative surface-wave inversion formulation based on the boundary element method (BEM) (see, for example, Brebbia and Dominguez, 1992) that overcomes the previously mentioned limitations of FEM-based FWIs, and at the same time still exploits a far more realistic modeling of the subsurface than the current state-of the-art SWMs. The proposed BEM-based FWI aims at filling the gap between the standard simplistic parallel-layered-based SWM and the more complex 3D FEM-based FWI, enabling an effective and better geometric characterization at any geological scale. The associated forward model is solved by the BEM, which is very effective for applications in which soil properties of the medium may be considered as regionally homogeneous (Beskos, Leung and Vardoulakis, 1986; Beskos, Dasgupta and Vardoulakis, 1986; Manolis and Beskos, 1988; Xu, 2001; Katsikadelis, 2002). Indeed, BEM was previously exploited to solve problems concerning structural vibration analysis, transient waves, and dynamics of cavities under the influence of body or surface waves (Manolis and Beskos, 1981, 1983; Beskos, Leung and Vardoulakis, 1986; Beskos, Dasgupta, and Vardoulakis, 1986; Manolis and Beskos, 1988) and to investigate the propagation of seismic waves in laterally varying layered media (Dineva and Manolis, 2001a, 2001b).

The proposed FWI approach is geometric because it infers the shape of 2D unknown irregular interfaces between regionally homogeneous soil layers directly from single-frequency measurements at the receivers, instead of an indirect inference from the observed dispersion curve, or an interpretation from maps of elastic properties estimated via FEM-based inversions. The elastic parameters are assumed to be given, but they can be easily estimated together with the geometric properties of the subsurface. This joint inversion is fairly straightforward and will be discussed elsewhere.

The paper is structured as follows: we first introduce the analytical formulation of the forward model for the wave propagation through 2D laterally varying layers and the associated numerical solution via BEM. Then a general inverse problem is introduced for the inference of subsurface interface geometries. To illustrate the potentialities of the geometric wave inversion, applications to benchmark problems and to a set of experimental data are finally presented.

BEM-Based Forward Model

Consider monochromatic waves at frequency ω propagating through a 2D subsurface made of N layers, as shown in Figure 1a. Let Ω_j be the generic layer bounded by the curve $\Gamma = \Gamma_{j-1} \cup \Gamma_j$, and x and z are the horizontal and vertical coordinates, respectively. In the frequency domain, the wave propagation in the generic j-th layer is governed by the

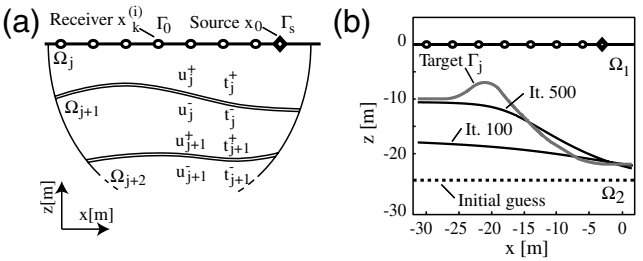

Figure 1. (a) Model setup and (b) BEM-based inversion of synthetic data on a two-layered media. Intermediate iterations show convergence to the target interface. No noise added to simulated measurements at the receivers.

following integral equation (Beskos, Leung and Vardoulakis, 1986):

$$\int_\Gamma \mathbf{U}^{(j)}(\mathbf{x},\mathbf{s},\omega)\mathbf{t}_{j(\mathbf{N})}(\mathbf{x},\omega)d\Gamma = \int_\Gamma \mathbf{T}^{(j)}(\mathbf{x},\mathbf{s},\omega)\mathbf{u}_j(\mathbf{x},\omega)d\Gamma + \mathbf{C}\mathbf{u}_j(\mathbf{x},\omega), \qquad \mathbf{x}\in\Gamma. \quad (1)$$

The fundamental tensors $\mathbf{U}^{(j)}$ and $\mathbf{T}^{(j)}$ are given in Dominiguez *et al.* (1984), and they depend upon the elastic parameters of the layer j, viz. density ρ_j, shear modulus μ_j, and Poisson's ratio ν_j. The (2×2) tensor $\mathbf{C}$ accounts for singular contributions of the Green tensor $\mathbf{U}^{(j)}$, when $\mathbf{x}=\mathbf{s}$, as well as for energy conservation in infinite domains (Dominiguez, 1993). Continuity of displacements and tractions at each interface requires that

$$\begin{aligned}\mathbf{u}_j^+(\mathbf{x},\omega) &= \mathbf{u}_j^-(\mathbf{x},\omega),\\ \mathbf{t}_{j(\mathbf{N}^+)}^+(\mathbf{x},\omega) &= -\mathbf{t}_{j(\mathbf{N}^-)}^-(\mathbf{x},\omega), \qquad \mathbf{x}\in\Gamma_j, \end{aligned} \quad (2)$$

for $j=1,\ldots N$, where $+$ and $-$ superscripts refer to the values of stresses or displacements at the upper and lower layers adjacent to the interface Γ_j, and $\mathbf{N}$ is the outward normal. Further, vanishing normal stress $\mathbf{t}_{0(\mathbf{N})}^-$ must be enforced at the free surface Γ_0, except at the source location $\mathbf{x}_0\in\Gamma_s$ where $\mathbf{t}_{0(\mathbf{N})}^- = f_0(\omega)\delta(\mathbf{x}-\mathbf{x}_0)\hat{\mathbf{z}}$, f_0 being the Fourier amplitude of the load along the normal $\hat{\mathbf{z}}$ to Γ_0, and $\delta(\mathbf{x})$ is the Dirac function. Hereafter, we drop denoting the dependence on ω, and the numerical approximation of equation (1) is obtained by discretizing each interface Γ_j in e_j quadratic isoparametric elements, along which the values of displacements and tractions are given, respectively, by

$$\begin{aligned}\mathbf{u}_j(\mathbf{x}) &= \sum_{n=1}^{3} P_n(\eta)\mathbf{u}_{k,n}^{(j)},\\ \mathbf{t}_{j(\mathbf{N})}(\mathbf{x}) &= \sum_{n=1}^{3} P_n(\eta)\mathbf{t}_{k,n}^{(j)}, \qquad \mathbf{x}\in\Gamma_{j,k}, \end{aligned} \quad (3)$$

where $\mathbf{u}_{k,n}^j$ and $\mathbf{t}_{k,n}^j$ are displacements and tractions vectors at the nth node on the kth element $\Gamma_{j,k}$, and $P_n(\eta)$ are interpolating functions with $\eta\in[-1,1]$. Using equation (3) and cycling the point of application of the fundamental tensors through all the nodes, a system of linear equations for the layer j follows as

$$[\mathbf{K}^{(j)}]\{\mathbf{u}^{(j)}\} = [\mathbf{G}^{(j)}]^{-1}[\mathbf{H}^{(j)}]\{\mathbf{u}^{(j)}\} = \{\mathbf{t}^{(j)}\}, \qquad j=1,\ldots N, \quad (4)$$

where the matrices $[\mathbf{G}^{(j)}]$ and $[\mathbf{H}^{(j)}]$ are given in Beskos, Leung, and Vardoulakis (1986), and the vectors $\{\mathbf{u}^{(j)}\}$ and $\{\mathbf{t}^{(j)}\}$ list displacements and tractions at the boundary nodes, respectively. These are degrees of freedom in a coordinate system local to the layer. Equation (4) is assembled by imposing the matching conditions of equation (2) following Beskos, Leung, and Vardoulakis (1986). The resulting linear system can be written in compact form as

$$[\mathbf{K}]\mathbf{u}_g = \mathbf{t}_g, \quad (5)$$

where $\mathbf{u}_g$ and $\mathbf{t}_g$ are global degrees of freedom with respect to the fixed coordinate system as shown in Figure 1. The solution of equation (5) follows after imposing loads and zero stresses at the free surface. Weight drop or sledgehammer are modeled in Fourier space as a nodal stress vector of intensity $f_0(\omega)$ and perpendicular to the free surface. For massive sources, such as an electromechanical shaker on a portion Γ_s of the free surface, the generated stress is given by $\mathbf{t}_s = m\omega^2\mathbf{d}_s + \mathbf{F}$, where the vectors $\mathbf{F}$ and $\mathbf{d}_s$ represent the force produced by the shaker and the displacements of Γ_s, respectively, with m being the shaker's mass. To test the numerical implementation of equation (4), we have considered the elastic problem of solving for the radial displacements on an infinitely long cylinder subject to a normal stress p. This admits an exact analytical solution given by Kitahara (1984). We set the elastic characteristics of the cylinder as $\rho = 100$ kg/m^3, $\mu = 10^6$ N/m^2, $\nu = 0.25$, damping ratio $\beta_r = 0.05$, and the normal load $f_0 = 100^2$ N/m^2. Figure 2 shows the BEM numerical stresses at two different resolutions and those expected from theory for $10 < \omega < 150$. The agreement with theory is remarkable (see also Dominguez, 1993). We point out that BEM can be easily generalized to multifrequency environments and 3D geometries. Further, viscoelasticity can be accounted for by the elastic-viscoelastic correspondence principle of linear viscoelasticity (Christensen, 1971; Manolis and Beskos, 1981).

Geometric BEM-Based Wave Inversion

Assume that the Fourier amplitudes $\mathbf{u}_{d_k}(\omega)$ of the vector displacements are known from measurements using N_{rec} receivers at $\mathbf{x}_k^{(r)}\in\Gamma_s$ and $k=1,\ldots N_{\text{rec}}$. Further, we focus

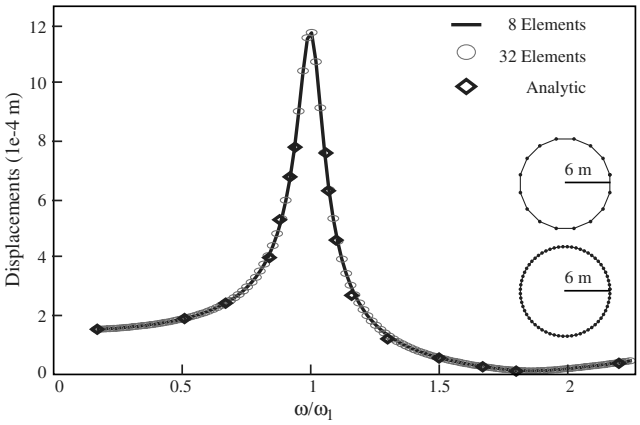

Figure 2. Radial displacements of an infinitely long cylinder subject to normal stress as function of the frequency ratio ω/ω_1: BEM versus analytical solution (Kitahara, 1984; Dominguez, 1993) (resonance frequency $\omega_1 = 59.73$ rad/s).

only on identifying the geometry of the boundary interfaces Γ_j and consider the elastic properties of the layers to be known *a priori*. We point out that these parameters could be easily estimated together with the geometry, but this will be discussed elsewhere. We consider an initially uniform discretization along $\hat{\mathbf{x}}$ using n_j nodes for each interface Γ_j, located at $\mathbf{x}_k^{(j)} = (x_k^{(j)}, z_k^{(j)})$, $k = 1, \ldots, n_j$. We calculate the optimal iterative displacement of these nodes by computing the first variation of the following energy functional:

$$\mathcal{E} = \frac{1}{2}\sum_{r=1}^{N_{\text{Rec}}} \|\mathbf{u}_k - \mathbf{u}_{d_k}\|^2 + \alpha \sum_{j=1}^{N_{\text{int}}} \sum_{k=1}^{e(j)} \int_{-1}^{1} \left[\left(\partial x_k^{(j)}/\partial\eta \right)^2 + \left(\partial z_k^{(j)}/\partial\eta \right)^2 \right]^{\frac{1}{2}} d\eta. \quad (6)$$

Here, the first term represents the mismatch between measured data at the receivers and the displacements $\mathbf{u}_k$ calculated from the forward model in equation (4), hereafter referred to as the misfit E. The second term is an arc-length regularizer that ensures smoothness of the boundary interface. This helps us avoid local minima of the energy represented in equation (6) due to measurement noise as well as avoid the ill-posedness of the problem when the number of degrees of freedom, $n_{\text{dof}} = \sum_{j=1}^{N_{\text{int}}} n_j$, exceeds the number of available measurements ($2N_{\text{rec}}$). N_{int} is the number of interfaces to be estimated, and $e(j)$ is the number of elements on the jth interface.

The energy functional in equation (6) depends nonlinearly on the interfaces and is therefore difficult to minimize directly. We apply an iterative deformation of an initial guessed interface by discretizing the continuous gradient descent flow obtained from the first variation of our energy functional $\mathcal{E}$. Let $\Gamma_j^{(0)}$ be an initial guess for the unknown (target) interface Γ_j, with nodal coordinates

$$\mathbf{x}_i = (x_i^{(j)}, z_{0,i}^{(j)}). \quad (7)$$

To minimize $\mathcal{E}$, we restrict the deformation of the curves to small perturbations along the vertical direction only by setting

$$z_i^{(j)} = z_{0,i}^{(j)} + \Delta_{z,i}^{(j)} \qquad \Delta_{z,i}^{(j)} \ll z_{0,i}^{(j)}. \quad (8)$$

Further, we indicate with Δ_p the inversion parameters corresponding to the $\Delta_{z,i}^{(j)}$ perturbations. The Taylor expansion of the displacements to the first order with respect to Δ_p is

$$\mathbf{u}_k = \mathbf{u}_k^{(0)} + \frac{\partial \mathbf{u}_k}{\partial \Delta_p}\Delta_p + O(\Delta_p^2), \qquad p = 1, \ldots, n, \quad (9)$$

where $O(\Delta_p^2)$ denotes the neglected higher-order terms of the series. Note that $\mathbf{u}_k^{(0)}$ is the BEM-solution for a geometry with interfaces $\Gamma_j^{(0)}$, and $\frac{\partial \mathbf{u}_k}{\partial \Delta_p}$ is the pth row of the Jacobian matrix $[\mathbf{J}]$, which measures the changes of the wave displacements at the receivers due to perturbations of the interfaces $\Gamma_j^{(0)}$. The matrix $[\mathbf{J}]$ is computed numerically via standard second order finite-differencing from equation (4). We anticipate that an adjoint solution (Eppstein *et al.*, 2003; Fedele *et al.*, 2003, 2005) was formulated for Helmholtz-type equations, and we are extending it to the Navier equations in order to efficiently compute $[\mathbf{J}]$ for $n_{\text{dof}} \gg 2N_{\text{rec}}$ using active surfaces (Yezzi *et al.*, 2002, 2003).

From equation (6),

$$\frac{\partial \mathcal{E}}{\partial \Delta_p} = \left(\frac{\partial \mathbf{u}_k}{\partial \Delta_p} \right)^T \left(\mathbf{u}_{k_0} + \frac{\partial \mathbf{u}_k}{\partial \Delta_p}\Delta_p - \mathbf{u}_{d_k} \right) + \alpha \sum_{n=1}^{N_{\text{int}}} \left(\sum_{i=1}^{n_j} r_{pi}\Delta_i + q_p \right), \quad (10)$$

where T denotes Hermitian transpose, and

$$r_{pi} = \sum_{k=1}^{n_e} \sum_{a,b=1}^{3} \int_{-1}^{1} (\gamma_k - \gamma_k^3 \phi_{z_k}^2) P'_a P'_b \delta_{bl} d\eta, \quad (11)$$

and

$$q_p = \sum_{k=1}^{n_e} \sum_{i=1}^{3} \int_{-1}^{1} \gamma_k \phi_{z_k} P'_i \delta_{il} d\eta, \qquad l = p - 2(k-1). \quad (12)$$

Here, δ_{nm} is the standard Kronecker delta, $\gamma_k = 1/\sqrt{\phi_{x_k}^2 + \phi_{z_k}^2}$, and

$$\begin{aligned} \phi_{x_k} &= P'_1(\eta) x_{0_{1,k}} + P'_2(\eta) x_{0_{2,k}} + P'_3(\eta) x_{0_{3,k}}, \\ \phi_{z_k} &= P'_1(\eta) z_{0_{1,k}} + P'_2(\eta) z_{0_{2,k}} + P'_3(\eta) z_{0_{3,k}}, \end{aligned} \quad (13)$$

where P' denotes a derivative of P with respect to η. The index k labels the interface elements, and l accounts for corresponding node elements. The optimal corrections Δ_p to reduce our energy functional from equation (6) are obtained by setting equation (10) to zero. This yields the optimal deformation $\boldsymbol{\Delta}_z$ as a solution of the linear system of equations, whose matrix form is given by Bignardi (2011):

$$\{[\mathbf{J}\mathbf{J}^T] + \alpha[\mathbf{R}]\}\boldsymbol{\Delta}_z = -[\mathbf{J}]\{\mathbf{u}_{k_0} - \mathbf{u}_{d_k}\} - \alpha\{\mathbf{q}\}, \quad (14)$$

where $\boldsymbol{\Delta}_z$ is a column vector that lists the vertical perturbations Δ_p, and the matrix entries in $[\mathbf{R}]$ and $\{\mathbf{q}\}$ are r_{pi} and q_p, respectively.

Thus, starting from an initial guess $\Gamma_j^{(0)}$ for the interfaces, the energy represented in equation (6) is minimized iteratively by evolving the interfaces according to equation (14), until the error $e_r = \max(|\Delta_p|)$ is smaller than a chosen tolerance ϵ. Relaxation is introduced to limit the increments Δ_p at each iteration by penalizing the squared norm of $\boldsymbol{\Delta}_z$. This adds an extra term $\beta[\mathbf{I}]$ to the left side of equation (14), where $[\mathbf{I}]$ is the identity matrix and β is a fixed constant. The weight

α of the regularizer is initially chosen large enough so that the algorithm reconstructs the coarser scale features of the curve; as the error e_r reduces, α is decreased to allow reconstruction of the finer scale features.

Applications

In the following we will test consistency and effectiveness of the geometric algorithm from equation (14) using synthetic data for the simple case of a one-layered geometry. Further, as a field-case study we present the inversion of an experimental data set collected at a site in Alabama in 2004.

Synthetic Data

Consider a 2D laterally varying layer on a half-space such as Figure 1b and a typical instrumentation setup for surface-wave testing at the geotechnical scale $\sim O(10)$ m. In particular, the receivers are equally spaced every 4 meters, and the source is located 3 meters away from the closest receiver. We assume to know the source, and the two different elastic characteristics of the two layers are considered. The first case represents a high acoustic impedance jump scenario with parameters $V_S = 150(800)$ m/s, $V_P = 500(2000)$ m/s, and $\rho = 1600(2200)$ kg/m^3 for the upper (lower) layer. The second case, on the other hand, represents a low impedance jump configuration with parameters $V_S = 150(250)$ m/s, $V_P = 500(1000)$ m/s, and $\rho = 1600(2000)$ kg/m^3. Further, the source intensity $f_0(\omega) = 1000\ N$ at frequency $\omega = 1$ rad/s. The laterally varying interface Γ should be inferred correctly (within given numerical accuracy) from both zero-noise horizontal and vertical displacements (data) collected at the seven receivers. Corrupted data may lead to estimates that deviate from the true interface, and such deviations will also be quantified. The unknown interface is discretized using 33 nodes. For the inversion, data at the receivers are simulated using the forward model from equation (4) and consist of complex Fourier amplitudes of both vertical and horizontal displacements. At first, no noise is added to data in order to test the convergence properties of the algorithm. The number of model parameters (33) is slightly larger than that of the available data (2×7). The arc-length regularizer in equation (6) guarantees a course-to-fine scale reconstruction of the unknown interface. The initial guessed interface Γ is set as horizontal at $z = -25$ m. Some of the intermediate iterates are shown in Figure 1 to illustrate the convergence toward the target interface. Observe that the iterated curve translates rigidly at the first few iterations as a result of the initially large arc-length regularization. As the iterations increase, the regularizer is reduced, and the curve deforms accordingly to adapt to the shape of the target interface in roughly 1500 iterations.

The algorithm runs in a MATLAB environment on a MacBook with an Intel dual core at 2.4 Ghz, and the computational time is about 40 s/iteration. An adjoint-based inversion is under development to speed up the algorithm (see, for example, Fedele *et al.*, 2003 and Eppstein *et al.*, 2003 for an application of adjoint methods in optical tomography). Further, implementation of the algorithm in a C^{++} environment will also reduce the computational burden.

To investigate the performance of the algorithm under noisy data, we added a Gaussian noise to the simulated measurements (both x and y components) with standard deviation $\sigma = (P/100)Q_{\max}/3$, with $P = 5\%$ as the noise percentage, and $Q_{\max}$ as the maximum value of the data (phase or amplitude) to be perturbed, which usually corresponds to the value recorded at the receiver with minimum offset. Note that the noise level of Fourier amplitudes corresponds to a larger error in the associated time-series displacements due to the nature of the Fourier transform. In particular, the algorithm still provides a good estimate of the true interface as shown in Figures 3 and 4, for the two previously mentioned cases of low and high impedance jumps. In the same figures, in order to appreciate convergence we also report the normalized misfit E/E_0 as a function of the number of iterations, with E_0 being the relative misfit of the initial guess. The inversion results are more sensitive, and thus less accurate, when noise is added to phases only (curve *P*) than when noise is added to amplitudes only (curve A), as clearly seen from the plots of the misfit errors in Figures 3–6. The largest separation along z between the estimated and target interfaces ranges from 1.2% to 8% with respect to the vertical extent of the dipping part of the layer, viz. $\Delta h = 15$ m. On the other hand, in field surveys only the vertical component of displacements is usually recorded. Thus, it is relevant to check the performance of the geometric algorithm when horizontal measurements are discarded in the inversion. Figure 5 shows the converged interfaces when noise is added only to phases (curve *P*) or amplitudes (curve *P*). Clearly, the

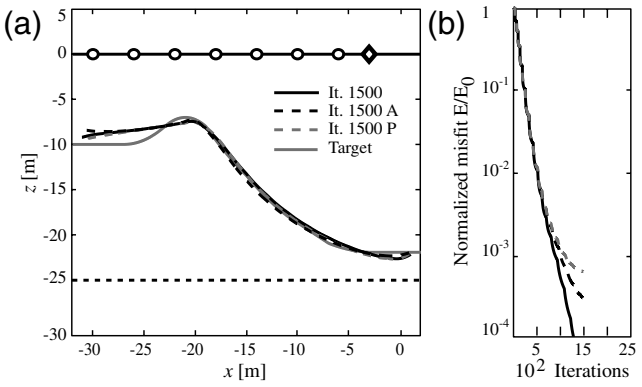

Figure 3. Sensitivity of the algorithm to noise level (5%): converged interfaces for unperturbed data, noisy amplitudes (A) or phases (P) only; (a) case of high acoustic impedance jump and (b) associated normalized misfits E/E_0 as functions of the number of iterations. Elastic parameters: $V_S = 150(800)$ m/s, $V_P = 500(2000)$ m/s, and $\rho = 1600(2200)$ kg/m^3 for the upper (lower) layer.

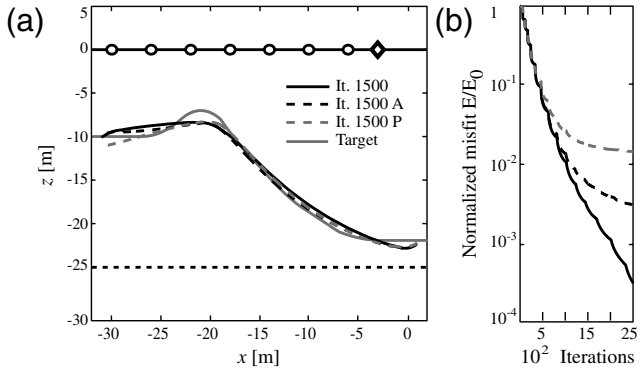

Figure 4. (a) Geometric inversion using vertical displacements only for unperturbed data, noisy amplitudes (A) and phases (P), respectively; (b) associated normalized misfit E/E_0 as a function of the number of iterations. Noise level 5%, high acoustic impedance jump case with elastic parameters: $V_S = 150(800)$ m/s, $V_P = 500(2000)$ m/s, and $\rho = 1600(2200)$ kg/m^3 for the upper (lower) layer.

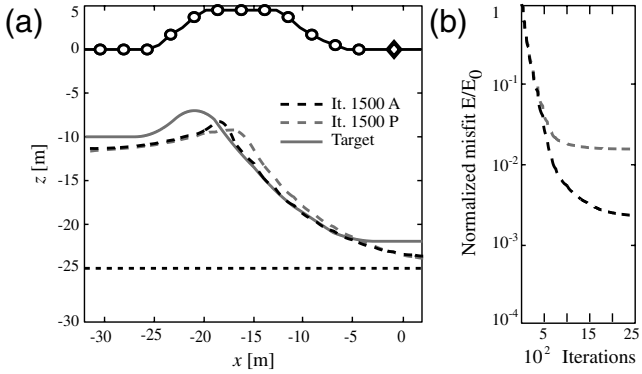

Figure 6. Boundary element method-based geometric inversion for geometries with nonflat free surfaces: reconstructed interfaces for corrupted amplitudes (A) and phases (P), respectively; (a) high acoustic impedance jump case and (b) associated normalized misfits E/E_0 as functions of the number of iterations. Elastic parameters: $V_S = 150(800)$ m/s, $V_P = 500(2000)$ m/s, and $\rho = 1600(2200)$ kg/m^3 for the upper (lower) layer.

geometric algorithm identifies the major features of the target interface, even if half of the data are discarded. In such conditions, the arc-length parameter α is decreased at a slower rate to yield a smoother course-to-fine evolution of the iterated curve. Moreover, a larger value of the Tikhonov parameter β is required to limit the correction of the curve at each iteration. As a result, the number of iterations has increased in comparison to the cases in which the entire set of data is exploited. The geometric algorithm can also handle irregular free surfaces in a natural manner, as clearly illustrated in Figures 6 and 7, where we report the reconstructed curves for data with noise level $P = 10\%$.

Observe that in all the inversions, we saw a remarkable agreement between data ($\mathbf{u}_d$) and the associated modeled values ($\mathbf{u}$), within the accuracy of measurements. For example, Figure 8 reports Fourier amplitudes and phases of measurements at the receivers in comparison with the associated estimated values for the inversion of Figure 3. Clearly, the BEM geometric algorithm is effective in reconstructing the interface Γ from noisy data.

Field-Case Study

We point out that the geometric algorithm is effective in estimating lateral interfaces, in particular, flat interfaces as a special case. To prove this, we considered an experimental data set collected at a site in Alabama in 2004. The experimental campaign was carried out using an electromechanical shaker equipped with an additional reactive mass that acts as

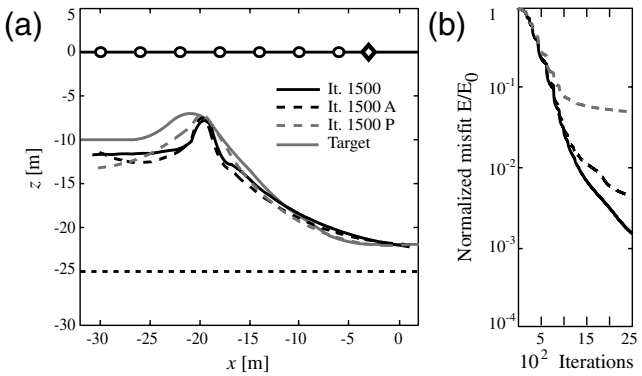

Figure 5. Sensitivity of the algorithm to noise level (5%): converged interfaces for unperturbed data, noisy amplitudes (A) and phases (P), respectively; (a) case of low acoustic impedance jump and (b) corresponding normalized misfits E/E_0 as functions of the number of iterations. Elastic parameters: $V_S = 150(250)$ m/s, $V_P = 500(1000)$ m/s, and $\rho = 1600(2000)$ kg/m^3 for the upper (lower) layer.

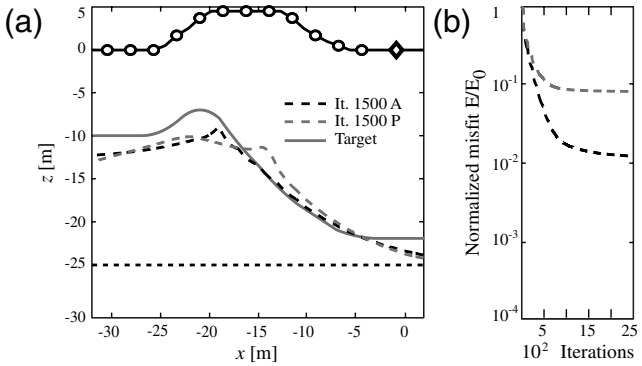

Figure 7. Boundary element method-based geometric inversion for geometries with nonflat free surfaces: reconstructed interfaces for corrupted amplitudes (A) and phases (P) respectively; (a) low acoustic impedance jump case and (b) corresponding normalized misfits E/E_0 as functions of the number of iterations. Elastic parameters: $V_S = 150(250)$ m/s, $V_P = 500(1000)$ m/s, and $\rho = 1600(2000)$ kg/m^3 for the upper (lower) layer.

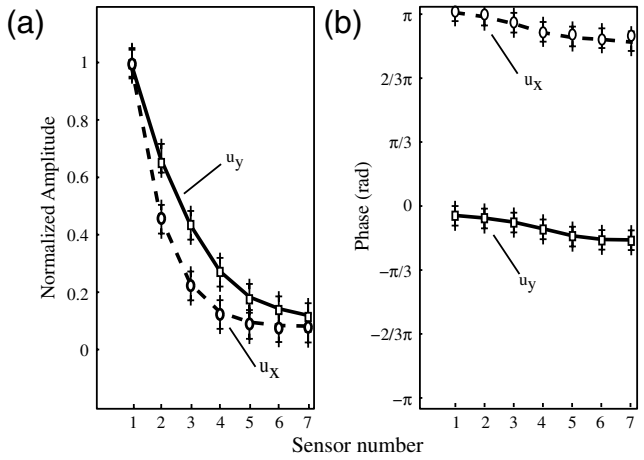

Figure 8. (a) Modeled normalized Fourier amplitudes of horizontal (vertical) displacements u_x (u_y) against data at the receivers for the case of noisy data with corrupted amplitudes only (see curve A of Fig. 3 for the associated reconstructed interface); (b) modeled phases against data at the receivers for noisy data with corrupted phases only (see curve P of Fig. 3 for the associated reconstructed interface). Noise level $P = 5\%$ and error bars denote stability bands of measurements.

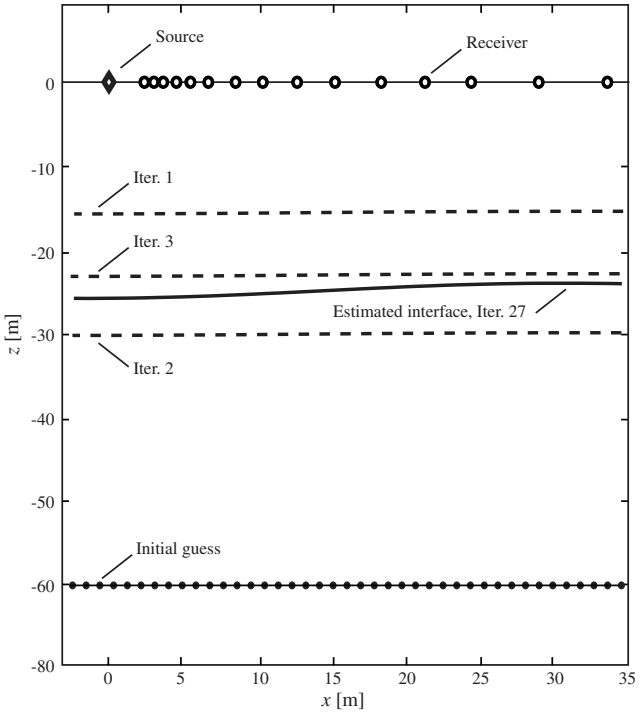

Figure 10. Geometric inversion of experimental data collected at the Alabama site. Elastic parameters: $V_S = 355(1370)$ m/s, $V_P = 664(2000)$ m/s, and $\rho = 1500(2400)$ kg/m^3 for the upper (lower) layer.

a harmonic source at frequencies ranging from ~3 to 100 Hz; therefore, these data are particularly indicated for one-frequency inversion. Vertical particle accelerations were measured by a linear array of 15 low-frequency accelerometers located at distances ranging from 2.4 to 32 meters from the source. Figure 9 shows the typical shear wave velocity profile estimated from conventional surface-wave testing on the field setup of Figure 10. We can approximate

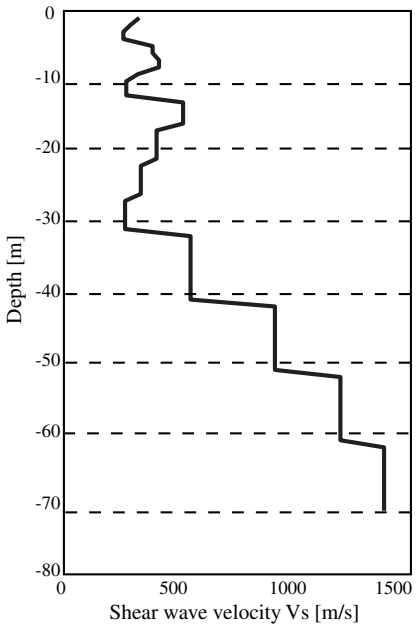

Figure 9. Local shear wave velocity profile estimated using standard SWMs at the Alabama site.

such geometry with that of a soft upper layer with thickness ~30 m laying on top of an half-space. An estimate of the shear velocity V_{S30} of the top layer is obtained from the profile of Figure 9 as

$$V_{S30} = \sum_{i=1}^{n_l} d_i \Big/ \sum_{i=1}^{n_l} \frac{d_i}{V_S(i)}, \tag{15}$$

where d_i and $V_S(i)$ are thickness and shear wave velocity of the ith layer, respectively, and similarly for that of the half-space. Further, remaining elastic parameters are inferred from some geological knowledge of the region. As a result, the elastic properties of the top layer (half-space) are set as $V_S = 335(1369)$ m/s, $V_P = 664(2001)$ m/s, and $\rho = 1500(2400)$ kg/m^3, respectively. To proceed with the inversion at the excitation frequency $\omega = 10$ Hz, we first computed the Fourier spectrum $S(w)$ of the measured vertical displacements, which is very narrow. Integrating the spectrum around ω over a window $\Delta w/\omega \sim 0.01$ (to filter out noise at lower and higher w's) provides the complex Fourier amplitudes at the receivers to be used as data in the BEM inversion. Here, the shaker force is modeled at the source node as $\mathbf{t}_s = m\omega^2\mathbf{d}_s + F_g\hat{\mathbf{z}}$, where F_g is the maximum force magnitude generated by the shaker, and m is the sum of reactive and device masses. The free surface Γ_s is discretized using 67 nodes, and the unknown interface Γ_1 is discretized with 41 nodes. The inverse problem is ill-posed because we

have 15 receivers and 41 unknowns, so the arc-length regularizer is needed. As shown in Figure 10, the initial guess of the unknown interface Γ_1 is set as horizontal at $z = -60$ m. The algorithm converged in 27 iterations, and some intermediates are shown in the same figure. Observe that in few iterations the iterate rigidly translates to nearby $z \sim -24$ m, then it shapes in to a very mild laterally varying interface, in good agreement with the local geology, which was previously known to be almost 1D. Shaping requires more iterations than translation as in the inversion of synthetic data (see Fig. 1).

The single-layer inversion provides an estimate of the location of the interface between the upper soft layer and the hard bottom at approximately $z \sim -24$ m. The model fit the data, as illustrated in Figure 11, where we report the modeled Fourier amplitudes and measurements at the receivers. Better agreement with data (especially for amplitudes) could be attained by performing the inversion with a multilayer geometry to have a better resolution of the softer, shallow layers of Figure 9. This is currently under investigation.

Conclusions

We have introduced a geometric inversion formulation that overcomes the stiffness of classic surface-wave methods in dealing with nonparallel subsurface layers. The inverse model exploits the BEM to infer the shape of 2D laterally varying interfaces directly from measurements at the receivers. No indirect inference is observed from the dispersion curve. Indeed, the proposed inverse algorithm exploits the ability of the BEM to model wave propagation through a medium whose soil properties may be approximated as regionally homogeneous. Tests on both synthetic and experimental data on 2D geometries provide evidence that the BEM-based geometric inversion is effective even in the presence of noise and is applicable for cases over large horizontal scales with steep interfaces, irregular free surfaces, and subsurfaces with low acoustic impedance ratios.

The method is easily generalizable to 3D geometries, and the estimated geometry provides a good initial guess for FEM-based FWIs in order to reconstruct higher-order structured heterogeneities. Thus, BEM-based inverse models have the potential to improve the effectiveness and accuracy of FEM-based inversions. Further, the BEM forward model can be accelerated using fast multipole techniques (Gumerov and Duraiswami, 2004; Liu, 2009), in combination with the use of adjoint methods to speed up the computation of the Jacobian, thus drastically reducing the computational burden of the algorithm.

We believe that the application of BEM-based inverse models to geological problems from small to large scales will enable researchers and other stakeholders to investigate the underground geological complexities with a low cost-to-benefits ratio method. Our preliminary results are very promising, with successbeing achieved in nicely reproducing an irregular interface in a 2D layered model. As far as the approach is in principle scale-invariant and has no space limitations, work is in progress to extend it for the inversion of multifrequency data and 3D multilayered geometries with inclusions or cavities. This will empower complete reconstructions of the subsurface in complex geological and tectonic structures at any scale.

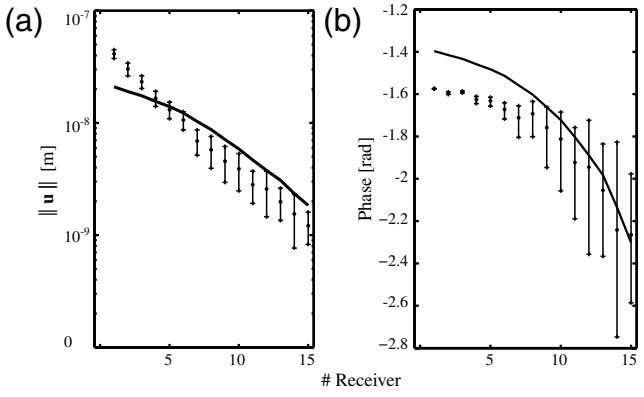

Figure 11. Field-case study: comparisons between data and model estimates at the receivers for the inversion of Figure 10. (a) Estimated normalized Fourier amplitudes and (b) associated phases against data (error bars denote stability bands of measurements).

Data and Resources

Available data were collected by G. J. Rix, and they cannot be shared publically.

References

Aki, K. (1988). Local site effects on strong ground motion, in Geotechnical Special Publication, N. 20, *Earthquake Engineering and Soil Dynamics II: Recent Advances in Ground Motion Evaluation*, J. L. Von Thun (Editor), American Society Civil Engineers, Park City, Utah.

Aki, K., and P. G. Richards (2002). *Quantitative Seismology, Theory and Methods*, Second Ed., University Science Books, Sausalito, California, 249–322.

Assimaki, D., and E. Kausel (2007). Modified topographic amplification factors for a single-faced slope due to kinematic soil-structure interaction, *J. Geotech. Geoenviron. Eng.* **133,** no. 11, 1414–1431.

Bard, P. Y. (1982). Diffracted waves and displacement field over two-dimensional elevated topographies, *Geophys. J. R. Astr. Soc.* **71,** 731–760.

Bard, P. Y., and J. C. Gabriel (1986). The seismic response of two-dimensional sedimentary deposits with large vertical velocity gradients, *Bull. Seismol. Soc. Am.* **76,** 343–366.

Beskos, D. E., B. Dasgupta, and I. G. Vardoulakis (1986). Vibration isolation using open or filled trenches, *Comput. Mech.* **1,** no. 1, 43–63.

Beskos, D. E., K. L. Leung, and I. G. Vardoulakis (1986). Vibration isolation of structures from surface waves in layered soil, *Rec. Appl. Comput. Mech.*, 125–140.

Bignardi, S. (2011). *Complete Waveform Inversion Approach to Seismic Surface Waves and Adjoint Active Surfaces*, *Ph.D. Thesis*, University of Ferrara, Ferrara, Italy.

Brebbia, C. A., and J. Dominguez (1992). *Boundary Elements, An Introductory Course*, WIT Press/Computational Mechanics Publications, Southampton, UK, 314 pp.

Christensen, R. M. (1971). *Theory of Viscoelasticity*, Academic Press, New York, 364 pp.

Dineva, P., and G. Manolis (2001a). Scattering of seismic waves by cracks in multi-layered geological regions: I. Mechanical model, *Soil Dynam. Earthq. Eng.* **21,** 615–625.

Dineva, P., and G. Manolis (2001b). Scattering of seismic waves by cracks in multi-layered geological regions: II. Numerical results, *Soil Dynam. Earthq. Eng.* **21,** 627–641.

Dominguez, J. (1993). *Boundary Elements in Dynamics*, Computational Mechanics Publications, Elsevier, Southampton, UK, 165–207.

Dominguez, J., and R. Abascal (1984). On fundamental solutions for the boundary integral equations method in static and dynamic elasticity, *Eng. Anal.* **1,** no. 3, 128–134.

Dravinski, M., and T. K. Mossessian (1987). Scattering of plane harmonic *P, SV,* and Rayleigh waves by dipping layers of arbitrary shape, *Bull. Seismol. Soc. Am.* **77,** no. 1, 212–235.

Eppstein, M., F. Fedele, J. P. Laible, C. Zhang, A. Godavarty, and E. M. Sevick-Muraca (2003). A comparison of exact and approximate adjoint sensitivities in fluorescence tomography, *IEEE Trans. Med. Imag.* **22,** no. 10, 1215–1222.

Fedele, F., M. Eppstein, J. P. Laible, A. Godavarty, and E. M. Sevick-Muraca (2005). Fluorescence photon migration by the Boundary Element Method, *J. Comput. Phys.* **210,** no. 1, 109–132.

Fedele, F., J. P. Laible, and M. Eppstein (2003). Coupled complex adjoint sensitivities for frequency-domain fluorescence tomography: Theory and vectorized implementation, *J. Comput. Phys.* **187,** no. 2, 597–619.

Fichtner, A. (2011). *Full Seismic Waveform Modelling and Inversion* Springer-Verlag, Heidelberg, Germany, 356 pp.

Gabriels, P., R. Snieder, and G. Nolet (1987). *In situ* measurements of shear-wave velocity in sediments with higher-mode Rayleigh waves, *Geophys. Prospect.* **35,** 187–196.

Gjevik, B. (1973). A variational method for Love waves in nonhorizontally layered structures, *Bull. Seismol. Soc. Am.* **63,** no. 3, 1013–1023.

Gumerov, N. A., and R. Duraiswami (2004). *Fast Multipole Methods for the Helmholtz Equation in Three Dimensions*, Elsevier Ltd., Oxford, UK, 520 pp.

Katsikadelis, J. T. (2002). *Boundary Elements: Theory and Applications* Elsevier Science, Oxford, UK, 201–234.

Kausel, E., and J. M. Roesset (1981). Stiffness matrices for layered soils, *Bull. Seismol. Soc. Am.* **71,** 1743–1761.

Kawase, H. (1988). Time-domain response of a semi-circular canyon for incident *SV, P* and Rayleigh waves calculated by the discrete wavenumber boundary element method, *Bull. Seismol. Soc. Am.* **78,** 1415–1437.

Kawase, H., and K. Aki (1989). A study of the response of a soft basin for incident *S, P,* and Rayleigh waves with special reference to the long duration observed in Mexico City, *Bull. Seismol. Soc. Am.* **79,** 1361–1382.

Kitahara, M. (1984). Applications of boundary integral equation methods to eigenvalue problems of elastodynamic and thin plates, *Research Report*, University of Kyoto, Kyoto, Japan.

Lai, C. G., G. J. Rix, S. Foti, and V. Roma (2002). Simultaneous measurement and inversion of surface wave dispersion and attenuation curves, *Soil Dynam. Earthq. Eng.* **22,** no. 9–12, 923–930.

Liu, Y. (2009). *Fast Multipole Boundary Element Method: Theory and Applications in Engineering*, Cambridge University Press **8,** New York, 5–118.

Louie, J. N. (2001). Faster, better: Shear-wave velocity to 100 meters depth from refraction microtremor arrays, *Bull. Seismol. Soc. Am.* **91,** no. 2, 347–364.

Luo, Y. H., J. H. Xia, J. P. Liu, Y. X. Xu, and Q. S. Liu (2008). Generation of a pseudo-2D shear-wave velocity section by inversion of a series of 1D dispersion curves, *J. Appl. Geophys.* **64,** 115–124.

Manolis, G. D., and D. E. Beskos (1981). Dynamic stress concentration studies by boundary integrals and Laplace transform, *Int. J. Numer. Meth. Eng.* **17,** no. 4, 573–599.

Manolis, G. D., and D. E. Beskos (1983). Dynamic response of lined tunnels by an isoparametric boundary element method, *Comput. Meth. Appl. Mech. Eng.* **36,** no. 3, 291–307.

Manolis, G. D., and D. E. Beskos (1988). *Boundary Element Methods in Elastodynamics*, Unwin Hyman Ltd., London, UK, 288 pp.

Maupin, V. (2007). Introduction to mode coupling methods for surface waves, *Adv. Geophys.* **48,** 127–155.

Maupin, V., and B. L. N. Kennett (1987). On the use of truncated modal expansions in laterally varying media, *Geophys. J. Int.* **91,** 837–851.

Nazarian, S., and K. H. Stokoe (1984). *In situ* shear wave velocity from spectral analysis of surface waves, *Proc. 8th Conf. on Earthquake Engineering*, Vol. **3**, Prentice Hall, San Francisco, California, 31–38.

Park, C. B., R. D. Miller, and J. Xia (1999). Multichannel analysis of surface waves, *Geophysics* **64,** 800–808.

Park, C. B., R. D. Miller, N. Ryden, J. Xia, and J. Ivanov (2005). Combined use of active and passive surface waves, *J. Environ. Eng. Geophys.* **10,** 323–334.

Raptakis, D., F. J. Chavez-Garcia, K. Makra, and K. Pitilakis (2000). Site effects at Euroseistest-I. Determination, of the valley structure and confrontation of observations with 1D analysis, *Soil Dynam. Earthq. Eng.* **19,** no. 1, 1–22.

Rix, G. J., G. L. Hebeler, and M. C. Orozco (2002). Near-surface *Vs* profiling in the New Madrid seismic zone using surface wave methods, *Seismol. Res. Lett.* **73,** no. 3, 380–392.

Rix, G. J., C. G. Lai, and A. W. Spang (2000). *In situ* measurement of damping ratio using surface waves, *J. Geotech. Geoenviron. Eng.* **126,** no. 5, 472–480.

Rix, G. J., C. G. Lai, and S. Foti (2001). Simultaneous measurement of surface wave dispersion and attenuation curves, *Geotech. Test. J.* **24,** no. 4, 350–358.

Savage, W. Z. (2004). An exact solution for effects of topography on free Rayleigh waves, *Bull. Seismol. Soc. Am.* **94,** no. 5, 1706–1727.

Stokoe, K. H., S. G. Wright, J. A. Bay, and J. M. Roesset (1994). Characterization of geotechnical sites by SASW method, *Proc. XIII Int. Conf. on Soil Mechanics and Foundation Engineering*, Oxford & IBH Publishing, New Delhi, India, 15–25.

Strobbia, C., and S. Foti (2006). Multi-offset phase analysis of surface wave data (MOPA), *J. Appl. Geophys.* **59,** 300–313.

Tarantola, A. (1987). *Inverse Problem Theory: Methods for Data Fitting and Model Parameter Estimation*, Elsevier, New York, 356 pp.

Tikhonov, A., and V. Arsenin (1977). *Solution of Ill-Posed Problems*, Wiley, New York.

Tokimatsu, K. (1995). Geotechnical site characterization using surface waves, *Proc. 1st Int. Conf. on Earthquake Geotechnical Engineering (IS-Tokyo '95)*, Balkema, Rotterdam, The Netherlands, 1333–1368.

Tselentis, G. A., and G. Delis (1998). Rapid assessment of *S*-wave profiles from the inversion of multichannel surface wave dispersion data, *Ann. Geofisc.* **41,** 1–15.

Virieux, J., and S. Operto (2009). An overview of full-waveform inversion in exploration geophysics, *Geophysics* **74,** no. 6, 127–152.

Xu, S. Z. (2001). *The Boundary Element Method in Geophysics*, in Geophysical Monograph Series, Society of Exploration Geophysicists, Tulsa, Oklahoma, 169–203.

Yezzi, A., A. Tsai, and A. Willsky (2002). A fully global approach to image segmentation via coupled curve evolution equations, *J. Vis. Comm. Image Represent.* **13,** 195–216.

Yezzi, A., L. Zollei, and T. Kapur (2003). A variational framework for integrating segmentation and registration through active contours, *Med. Image Anal.* **7,** 171–185.

Appendix

BEM Matrices

$$[\boldsymbol{H}] = \begin{Bmatrix} [\mathcal{T}^1_{11}][\mathcal{T}^1_{12}][\mathcal{T}^1_{13}+\mathcal{T}^1_{21}][\mathcal{T}^1_{22}] & \cdots \\ [\mathcal{T}^2_{11}][\mathcal{T}^2_{12}][\mathcal{T}^2_{13}+\mathcal{T}^2_{21}][\mathcal{T}^2_{22}] & \\ [\mathcal{T}^3_{11}][\mathcal{T}^3_{12}][\mathcal{T}^3_{13}+\mathcal{T}^3_{21}][\mathcal{T}^3_{22}] & \\ [\mathcal{T}^4_{11}][\mathcal{T}^4_{12}][\mathcal{T}^4_{13}+\mathcal{T}^4_{21}][\mathcal{T}^4_{22}] & \\ \vdots & \ddots \\ & [\mathcal{T}^{n_j}_{(n_e-1)\mathbf{3}}+\mathcal{T}^{n_j}_{n_e\mathbf{1}}][\mathcal{T}^{n_j}_{n_e\mathbf{2}}][\mathcal{T}^{n_j}_{n_e\mathbf{3}}] \end{Bmatrix}, \tag{A1}$$

and

$$[\boldsymbol{G}] = \begin{Bmatrix} [\mathcal{U}^1_{11}][\mathcal{U}^1_{12}][\mathcal{U}^1_{13}+\mathcal{U}^1_{21}][\mathcal{U}^1_{22}] & \cdots \\ [\mathcal{U}^2_{11}][\mathcal{U}^2_{12}][\mathcal{U}^2_{13}+\mathcal{U}^2_{21}][\mathcal{U}^2_{22}] & \\ [\mathcal{U}^3_{11}][\mathcal{U}^3_{12}][\mathcal{U}^3_{13}+\mathcal{U}^3_{21}][\mathcal{U}^3_{22}] & \\ [\mathcal{U}^4_{11}][\mathcal{U}^4_{12}][\mathcal{U}^4_{13}+\mathcal{U}^4_{21}][\mathcal{U}^4_{22}] & \\ \vdots & \ddots \\ & [\mathcal{U}^{n_j}_{(n_e-\mathbf{1})3}+\mathcal{U}^{n_j}_{n_e\mathbf{1}}][\mathcal{U}^{n_j}_{n_e\mathbf{2}}][\mathcal{U}^{n_j}_{n_e\mathbf{3}}] \end{Bmatrix}. \tag{A2}$$

Further,

$$\begin{aligned} [\mathcal{U}^s_{kn}]_{ji} &= \int_{-1}^{1} U_{ji}[\mathbf{x}_k(\eta), \mathbf{x}_s, \omega] P_n(\eta) J(\eta) d\eta, \\ [\mathcal{T}^s_{kn}]_{ji} &= \int_{-1}^{1} T_{ji}[\mathbf{x}_k(\eta), \mathbf{x}_s, \omega] P_n(\eta) J(\eta) d\eta \end{aligned} \tag{A3}$$

Here, $U_{ji}(\mathbf{x}_k(\eta), \mathbf{x}_s, \omega)$ is the 2×2 fundamental tensor whose entries represent the i component of displacements at $\mathbf{x}_k(\eta)$ on the element k due to a Dirac source at $\mathbf{x}_s$ directed along j where $i, j = 1$ or 2 (x or z directions). Further, $\mathcal{U}^s_{kn}$ is the fundamental tensor U_{ji} projected onto the element $k \in [1, n_e]$ at the node $n \in \{1, 2, 3\}$ with a Dirac source at the node $s \in [1, n_j]$. Finally, the Lagrangian interpolation functions and Jacobian are defined, respectively, as

$$\begin{aligned} P_1(\eta) &= -1/2\eta + 1/2\eta^2, \\ P_2(\eta) &= 1 - \eta^2, \\ P_3(\eta) &= 1/2\eta + 1/2\eta^2, \end{aligned} \tag{A4}$$

and

$$J = \sqrt{\left(\sum_{i=1}^{3} \frac{dP_i}{d\eta} x_i\right)^2 + \left(\sum_{i=1}^{3} \frac{dP_i}{d\eta} z_i\right)^2}, \tag{A5}$$

with (x_i, z_i) as the nodal coordinates.

Department of Earth Science
University of Ferrara
Università degli Studi di Ferrara
Dipartimento di Scienze della Terra
Via Saragat 1 (Edicio B), 44122 Ferrara, Italy
(S.B., G.S.)

School of Electrical and Computer Engineering
Georgia Institute of Technology
225 North Avenue NW
Atlanta, Georgia 30332
(F.F., A.Y.)

School of Civil and Environmental Engineering
Georgia Institute of Technology
225 North Avenue NW
Atlanta, Georgia 30332
(G.R.)

Manuscript received 29 March 2011